Non-linearity in a Cavity QED system due to Rydberg excitations

LEE Chern Hui

An academic exercise presented in partial fulfillment for the degree of
Bachelor of Science with Hornours in Physics

Supervisor: Assoc. Prof. Murray BARRETT

Department of Physics

NATIONAL UNIVERSITY OF SINGAPORE

Abstract

We study experimentally the non-linearity of the Jaynes-Cummings model induced by the presence of Rydberg excitations within an atomic ensemble. The experimental setup is built, including an optical cavity of finesse $\mathcal{F} = 900$, the vacuum system and the major laser systems. Rubidium atoms are succesfully trapped in a cavity-assited optical dipole trap. Preliminary result on the measurement of the dispersive shift of the cavity is discussed.

Contents

Chapter 1

Introduction

Quantum Information and Computation (QIC) has received a great deal of attention as it promises much higher efficiency in performing certain classes of tasks as compared to classical computers [1, 2]. A quantum computer, in analogy with a classical one, is made up of information stored in quantum bits (or qubits) and a series of quantum logic gates which act on these qubits to generate the outputs of algorithms. The realization of a large-scale quantum computer would require many qubits. However, the technical difficulty of storing and manipulating many qubits in a single quantum system increases rapidly with their number. One of the proposed solutions to realizing a large-scale quantum computer is the quantum network. A quantum network consists of many quantum nodes that store and process relatively smaller numbers of qubits locally and are linked to each other through quantum channels [3]. In this framework, atomic systems naturally serve as local memory for the storage of information, while photons serve as the information carriers in the quantum channels. Photons are particularly suited as information carriers by virtue of their ease of transport over long distances and their imperviousness to decoherence [1]. Photons are insensitive to decoherence because they normally interact very weakly with other systems and among themselves. While this is advantageous for an information carrier, it makes it difficult to realize the interactions required for quantum logic gates using single photons.

One means of achieving the required interaction strength is to use an optical cavity to mediate the interaction between the photonic and atomic systems. Owing to the high reflectivity of the mirrors that constitute the cavity, the dipole interaction between the atom and the electromagnetic field is significantly enhanced due to the multiple passes made by a single photon within the resonator. This so-called cavity quantum-electrodynamics

(CQED) system is well-described by the Jaynes-Cummings model [4] which predicts a characteristic optical non-linearity at the single photon level. This non-linearity is most clearly manifest in the 'photon-blockade' effect whereby after a single photon enters the cavity, subsequent incident photons are reflected. This effect has been experimentally observed [5] and demonstrates the capability for effective photon-photon interactions mediated via the atom-cavity system. Such photon-photon interaction are a critical resource for a deterministic optical quantum computer [1], for example enabling the realization of an optical C-NOT gate [6]. Many experiments have used strong coupling between a single atom and photon inside a high-finesse optical cavity to demonstrate the basic processes required for quantum computation [5, 7, 8, 9].

To achieve this so-called 'strong-coupling' regime between a single atom and the cavity field, a cavity of sufficiently high finesse is required. This poses a technological barrier due to the difficulty in cavity manufacture and the sensitivity of these cavities to defects such as birefringence[5]. Furthermore, these experiments are notoriously complex and lossy; limiting their scalability and practical application. One possibility to improve the situation is to instead use an ensemble of N atoms and relax to requirements on the cavity finesse. Having N atoms coupled to a single cavity mode enhances the coupling strength by a factor of $\sqrt{N}$. The downside is that the N-atom system can now absorb multiple excitations, as opposed to the single atom situation, and the non-linear features of the Jaynes-Cummings model are no longer present. So while an ensemble-cavity system benefits from enhanced coupling and low losses, which are useful for some QIC applications such a efficient quantum memories [10] and on-demand photon sources [11], there is limited scope for realizing quantum optical non-linearities in this system.

Aside from strong-coupling optical resonators, another promising means of realizing an strong optical non-linearity is to use the dipole-dipole interaction between Rydberg states. Rydberg states are highly excited atomic states with high principle quantum number (typically $n \gtrsim 20$). Electrons in Rydberg states have orbitals far from the nuclei, resulting in a high polarizability. Although the van Der Waals potential is normally weak and neglected, it scales as n^{11} [12]. Thus Rydberg atoms interact strongly over relatively long distances ($\sim 10\,\mu\mathrm{m}$) through the van Der Waals potential. Consequently, when a single atom is excited by a laser to a Rydberg state, nearby atoms experience an energy shift which prevents a second atom from excitation to the Rydberg state. This is known as the 'Rydberg-blockade' effect and is clearly analogous to the above mention 'photon-blockade' effect of CQED. The Rydberg-blockade effect has been used to demonstrate strong optical non-linearities in free-space atomic ensembles [13, 14].

The aim of this experiment is to investigate quantum optical non-linearity in a hybrid

system consisting of an atomic ensemble in a cavity with Rydberg excitation. Ideally, one can consider an ensemble for which a single Rydberg excitation prevents absorption of any further excitations by the entire ensemble. Inside a cavity, this ensemble could be considered as a single 'super-atom' which can only absorb one excitation but has a collectively enhanced coupling to the cavity. This hybrid system can be formally reduced to a Jaynes-Cummings description with an ultra-strong effective coupling [15]. Using state-of-the-art high finesse mirrors, one could realize non-linearities far stronger than previous single-atom cavity experiments. Even using more readily accessible moderate finesse cavity mirrors and ensemble sizes [16, 17], one can reach an interesting quantum non-linear regime. In our first attempt to study this hybrid system, we have opted a build a cavity of only moderate finesse ($F \approx 1000$) to make experiment more technically feasible.

This report summarizes a year-long project which consisted largely of constructing the experimental apparatus and preliminary measurements in preparation the above experiment. The structure is as follows: in chapter 2, the theoretical aspects of the project will be presented, including the general results of cavity QED which will subsequently be used in the analysis of our experimental result. The construction of the necessary tools for the experiment will be presented in detail in chapter 3. Chapter 4 is devoted to the preparation of the cold atomic cloud in the experiment. In chapter 5, the cavity probing process will be presented together with some preliminary experimental results. The conclusions and discussions on the future plan of the project will be presented at the end of the report.

Chapter 2

Cavity QED with Rydberg atoms

In this chapter, I will first discuss some general results of cavity QED that are relevant to the experiment, followed by the introduction of the dispersive regime and the role of Rydberg atoms in the cavity system.

2.1 General Framework of Cavity QED

In a general cavity QED setup, we have a two-level system interacting with a single cavity mode. The energies of the individual cavity and atom can be written as

$$\begin{aligned}\hat{H}_0 &= \hbar\omega_0|\mathrm{e}\rangle\langle\mathrm{e}| + \hbar\omega_c\hat{a}^\dagger\hat{a} \\ &= \hbar\omega_0|\mathrm{e}\rangle\langle\mathrm{g}|\,|\mathrm{g}\rangle\langle\mathrm{e}| + \hbar\omega_c\hat{a}^\dagger\hat{a} \\ &= \hbar\omega_0\hat{\sigma}^\dagger\hat{\sigma} + \hbar\omega_c\hat{a}^\dagger\hat{a} \qquad ,\end{aligned} \tag{2.1}$$

where $\hat{\sigma} = |\mathrm{g}\rangle\langle\mathrm{e}|$ is the atomic lowering operator, $\hat{a}$ is the annihilation operator for the cavity mode. The quantized intracavity electric field polarized along the vector $\boldsymbol{\epsilon}$ is described by the operator

$$\hat{\mathbf{E}} = \boldsymbol{\epsilon} f(\mathbf{r})\,\mathcal{E}\left(\hat{a} + \hat{a}^\dagger\right) \qquad , \tag{2.2}$$

where $\mathcal{E}$ is the field amplitude for single cavity photon, and $f(\mathbf{r})$ describes the cavity spatial mode, with $\int \mathrm{d}^3\mathbf{r}\; f(\mathbf{r})^2 = V_m$ is the cavity mode volume.

The atom interacts with the cavity mode via the dipole interaction

$$\begin{aligned}\hat{H}_{\text{interaction}} &= -\hat{\mathbf{d}} \cdot \hat{\mathbf{E}} \\ &= -\left(\mathbf{d} \cdot \boldsymbol{\epsilon}\right) \mathcal{E} f(\mathbf{r}) (\hat{\sigma} + \hat{\sigma}^\dagger)(\hat{a} + \hat{a}^\dagger) \qquad ,\end{aligned} \tag{2.3}$$

and we define the atom-cavity coupling constant

$$g(\mathbf{r}) = \frac{-\left(\mathbf{d} \cdot \boldsymbol{\epsilon}\right) \mathcal{E} f(\mathbf{r})}{\hbar} \qquad .$$

The total Hamiltonian is then

$$\begin{aligned}\hat{H} &= \hat{H}_0 + \hat{H}_{\text{interaction}} \\ &= \hbar\omega_0 \hat{\sigma}^\dagger \hat{\sigma} + \hbar\omega_c \hat{a}^\dagger \hat{a} + \hbar g (\hat{\sigma} + \hat{\sigma}^\dagger)(\hat{a} + \hat{a}^\dagger) \qquad .\end{aligned}$$

Making the rotating wave approximation, we drop the fast oscillating terms and the resulting Hamiltonian takes the form of the Jaynes-Cummings Model (JCM)

$$\hat{H} = \hbar\omega_0 \hat{\sigma}^\dagger \hat{\sigma} + \hbar\omega_c \hat{a}^\dagger \hat{a} + \hbar g \left(\hat{a}\hat{\sigma}^\dagger + \hat{a}^\dagger \hat{\sigma}\right) \qquad . \tag{2.4}$$

The interaction Hamiltonian describes the coherent exchange of excitations between the atom and the cavity and it induces coupling only between states containing the same number of excitations, $|\mathrm{e}, n\rangle$ and $|\mathrm{g}, n+1\rangle$. Being the only state with zero excitation, the ground state $|\mathrm{g}, 0\rangle$ is therefore decoupled from the others. For the subspace with $(n+1)$ excitations, the new eigenbasis and eigenenergies are then

$$\begin{cases} E_n^{(+)} &= (n+1)\hbar\omega_c - \frac{1}{2}\hbar\Delta + \frac{\hbar}{2}\sqrt{\Delta^2 + (2g_n)^2} \\ |+\rangle_n &= \sin\theta_n |\mathrm{e}, n\rangle + \cos\theta_n |\mathrm{g}, n+1\rangle \end{cases} \tag{2.5a}$$

$$\begin{cases} E_n^{(-)} &= (n+1)\hbar\omega_c - \frac{1}{2}\hbar\Delta - \frac{\hbar}{2}\sqrt{\Delta^2 + (2g_n)^2} \\ |-\rangle_n &= \cos\theta_n |\mathrm{e}, n\rangle - \sin\theta_n |\mathrm{g}, n+1\rangle \end{cases} \tag{2.5b}$$

where $\Delta = \omega_c - \omega_0$ is the cavity detuning, $g_n = g\sqrt{n+1}$ is the effective coupling strength between the two states in the $(n+1)$-th excitation subspace, and the mixing

angles

$$\cos 2\theta_n = \frac{\Delta}{\sqrt{\Delta^2 + (2g_n)^2}} \quad \text{, and} \quad \sin 2\theta_n = \frac{2g_n}{\sqrt{\Delta^2 + (2g_n)^2}}.$$

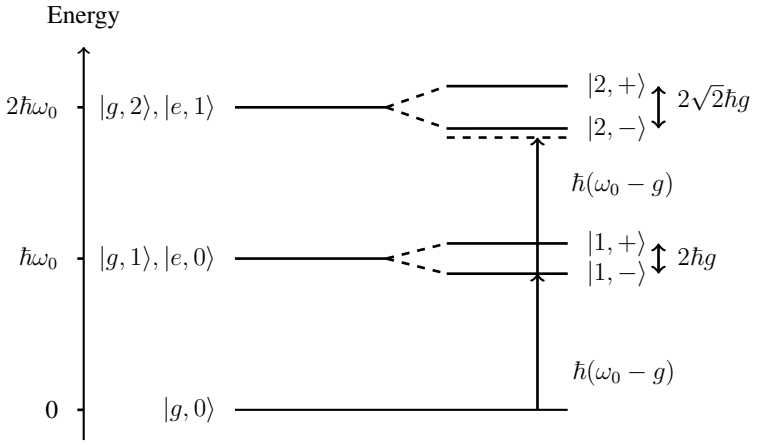

Figure 2.1: Energy diagram of the first few levels of the Jaynes-Cummings Model for $\omega_c = \omega_0$. The two arrows indicate the path if two photons of the same frequency $(\omega_0 - g)$ were absorbed. Notice that the absorption of the second photon is not resonant, hence the excitation spectrum is non-linear.

As can be seen from Eq. (2.5) and depicted in Fig. 2.1, the energy separation between the two eigenstates within the subspace of n excitations increases with n. The combined atom-cavity system is therefore highly non-linear. As shown in Fig. 2.1, for the case of $\Delta = 0$, it is impossible to excite the system with the same amount of energy once it is already in the excited state. This blockade effect is useful for example in creating a controlled-phase flip gate [6] and its observation has been reported in [8].

2.1.1 Far-detuned Regime and Dispersive Shift

In the presence of very few excitations, the analysis can be limited to the lowest subspace with $n = 1$. In the regime where the cavity is far-detuned from the atomic transition,

$\Delta \gg g$, the two eigenenergies in Eq. (2.5) reduce to

$$E_1^{(+)} = \hbar\omega_+ \qquad \text{with } \omega_+ = \left(\omega_c + \frac{g^2}{\Delta}\right) \tag{2.6a}$$

$$E_1^{(-)} = \hbar\omega_- \qquad \text{with } \omega_- = \left(\omega_0 - \frac{g^2}{\Delta}\right) \tag{2.6b}$$

In order to drive the system efficiently, the driving frequency needs to be close to one of these two eigenfrequencies. At ω_+, the system is 'cavity-like' and it responds strongly to a cavity driving force. When the cavity is driven by an external light source such as a laser beam, the beam enters the cavity only when the laser's frequency is close to ω_+ and a peak in the cavity's transmission is expected. On the other hand, at ω_-, the system is 'atom-like' and it responds to an atomic driving force, for example when the atom is pumped directly by a laser, the excitation probability of the atom peaks at ω_- instead of ω_0.

The 'cavity-like' frequency ω_+ is shifted from the empty cavity resonant frequency ω_c by g^2/Δ. This shift is referred to as the dispersive shift.

$$\Delta_{\text{Disp}} = \frac{g^2}{\Delta} \tag{2.7}$$

The shift is purely a dispersive effect as the driving field is weak and far-detuned from the atomic transition thus very little excitation probability is expected. Another way to view this is that the introduction of an atom in the cavity changes the refractive index of the cavity, inducing an additional phase shift per round-trip. This phase shift is translated into a in resonance frequency as if the length of the cavity was altered.

For the eigenstate $|+\rangle$ in the far-detuned regime, the probability of finding the atom in the excited state falls off as g/Δ. Therefore, working in this dispersive regime lowers the excited state population and the scattering rate into free space – a process that contributes to the loss of signal and decoherence.

2.1.2 Collective Coupling of $N \gg 1$ atoms

Suppose now we have N atoms coupled to the same cavity mode, the coupling strength will be enhanced [18]. If the mutual interaction between the atoms is negligible, the JCM Hamiltonian becomes the Tavis-Cummings Hamiltonian

$$\hat{H} = \hbar\omega_c \hat{a}^\dagger \hat{a} + \hbar\omega_0 \sum_{i=1}^{N} \hat{\sigma}_i^\dagger \hat{\sigma}_i + \hbar \sum_{i=1}^{N} g(\mathbf{r}_i) \left(\hat{a}\hat{\sigma}_i^\dagger + \hat{a}^\dagger \hat{\sigma}_i \right) \quad . \tag{2.8}$$

We can define the collective lowering and raising operators

$$\hat{S} = \frac{1}{\sqrt{N}} \sum_{i=1}^{N} \frac{g(\mathbf{r}_i)}{\bar{g}} \hat{\sigma}_i \,, \quad \hat{S}^\dagger = \frac{1}{\sqrt{N}} \sum_{i=1}^{N} \frac{g(\mathbf{r}_i)}{\bar{g}} \hat{\sigma}_i^\dagger \quad \text{where } \bar{g} = \sqrt{\frac{1}{N} \sum_{i=1}^{N} g(\mathbf{r}_i)^2}.$$

In the subspace of low excitation number,

$$\begin{aligned} \left[\hat{S}, \hat{S}^\dagger \right] &= \frac{1}{N\bar{g}^2} \sum_{i=1}^{N} g(\mathbf{r}_i)^2 \left(|\mathrm{g}_i\rangle\langle \mathrm{g}_i| - |\mathrm{e}_i\rangle\langle \mathrm{e}_i| \right) \\ &\approx \frac{1}{N\bar{g}^2} \sum_{i=1}^{N} g(\mathbf{r}_i)^2 \; \mathbb{1} \\ &= 1 \end{aligned}$$

Transforming into the interaction picture, the Hamiltonian becomes

$$\tilde{H} = \hbar\sqrt{N}\bar{g} \left(\hat{a}\hat{S}^\dagger e^{i(\omega_0 - \omega_c)t} + \hat{a}^\dagger \hat{S} e^{-i(\omega_0 - \omega_c)t} \right) \quad . \tag{2.9}$$

Hence, the system behaves like two coupled harmonic oscillators, defined by the annihilation operators $\hat{a}$ and $\hat{S}$, of frequency ω_c and ω_0 respectively, with coupling strength $\sqrt{N}\bar{g}$. It is easily verified that for $\omega_c = \omega_0$ the states

$$|\pm^{(1)}\rangle = \frac{1}{\sqrt{2}} \left(|\mathrm{G}^{(N)}\rangle \otimes |1\rangle \pm |\mathrm{E}^{(N)}\rangle \otimes |0\rangle \right) \qquad \text{with}$$

$$\begin{cases} |\mathrm{E}^{(N)}\rangle \equiv \frac{1}{\sqrt{N}} \sum_{i=1}^{N} \frac{g(\mathbf{r}_i)}{\bar{g}} |\mathrm{g}_1, \mathrm{g}_2, \ldots, \mathrm{g}_{i-1}, \mathrm{e}_i, \mathrm{g}_{i+1}, \ldots, \mathrm{g}_N\rangle \\ |\mathrm{G}^{(N)}\rangle \equiv |\mathrm{g}_1, \mathrm{g}_2, \ldots, \mathrm{g}_N\rangle \end{cases}$$

are eigenstates of Eq. (2.8) in the subspace of one excitation, with eigenenergies $E_\pm^{(1)} =$

$\hbar\omega_0 \pm \hbar\sqrt{N}\bar{g}$. The analytic solution for this Hamiltonian is more algebraically involved for the subspaces with higher number of excitation, and is provided in [19]. From Eq. (2.9) we expect to have $(n+1)$ levels in the subspaces with $n \ll N$ excitations.

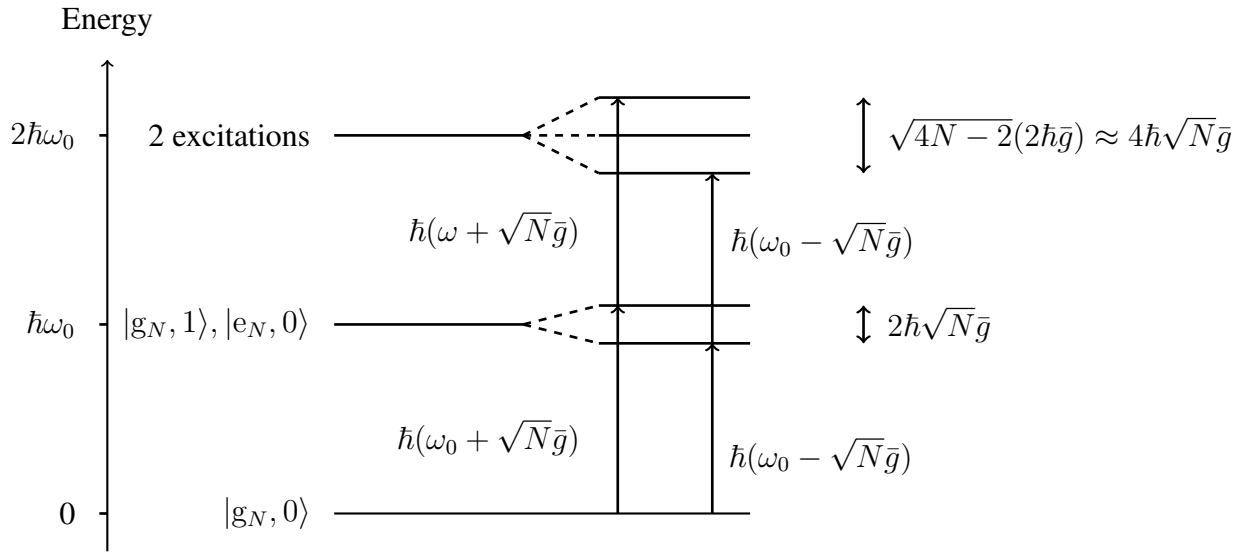

Figure 2.2: Energy diagram of the first few levels of the Tavis-Cummings model with $\omega_c = \omega_0$.

In the absence of mutual interaction, the atomic ensemble can now accept more than one excitation and the non-linearity in the JCM is destroyed at low number of excitations. However, due to the coupling between the cavity mode and the ensemble, the dispersive shift is always observed in the far-detuned regime. Compared to Eq. (2.7), the light in the cavity experiences a phase shift from each of the N atoms and the total dispersive shift is therefore

$$\Delta_{\text{Disp}} = \frac{N\bar{g}^2}{\Delta} \quad . \tag{2.10}$$

2.2 Role of Rydberg Atoms in the Cavity QED system

The analysis presented in this section follows the proposal by Guerlin et al. [15]. If the atomic upper state is now coupled via another strong classical beam with Rabi frequency Ω to a Rydberg excited state, the result will be very different.

2.2.1 Rydberg Blockade Effect

Rydberg states are highly excited atomic states with high principle quantum number (normally $n \gtrsim 20$). Electrons in Rydberg states have orbitals far from the nuclei, resulting in a large polarizability. The dipoles of such highly excited atoms interact strongly through the van Der Waals potential. The van Der Waals potential is of the form

$$V(\mathbf{r}) = \frac{C}{r^6}$$

and is normally weak and neglected as it falls off rapidly with increasing interatomic distance. However, the constant C scales as n^{11} [12], and thus for atomic states with high principle quantum numbers, the range of interaction is significantly increased. This range of interaction is called the Rydberg blockade range, ℓ_R, and is on the order of micrometers for Rydberg states of $n \gtrsim 70$ in Rubidium-87 [15].

In an atomic ensemble, the configuration with more than one Rydberg atom in the spherical region of radius ℓ_R would result in an additional energy shift due to the van Der Waals repulsive interaction. When the ensemble is excited by a laser to a Rydberg level, this additional energy shift effectively prohibits the ensemble from being doubly excited due to the insufficient energy of a light quantum. The ensemble can then be regarded as a 'two-level atom' with the excited state being the symmetric superposition of configurations with exactly one Rydberg atom. This is called the Rydberg blockade effect.

2.2.2 Effective Hamiltonian

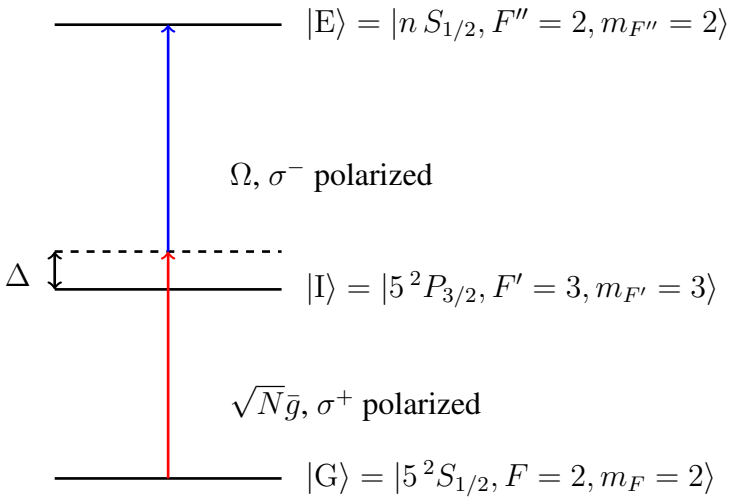

Figure 2.3: Two-photon process coupling the ground state to a Rydberg level. The diagram is specifically drawn with our experimental configuration for ^{87}Rb.

Following the development in Sec. 2.1.2, we can now replace the process by a two-photon transition as depicted in Fig. 2.3. The cavity resonance is far-detuned from the transition from the ground state to the intermediate state, $\Delta \gg \gamma_{\mathrm{I}}$. After adiabatically eliminating the intermediate state, the effective interaction Hamiltonian is [15]

$$\tilde{H}_{\text{eff}} = \hbar \frac{\sqrt{N}\bar{g}\Omega}{2\Delta} \hat{a}\hat{S}^\dagger + \text{H.c.}$$

where 'H.c.' stands for the hermitian conjugate. The system is back to the JCM because the atomic ensemble cannot be doubly excited due to the Rydberg blockade mechanism, but with an atom-cavity coupling strength enhanced by a factor of $\sqrt{N}$

$$g_{\text{eff}} = \frac{\sqrt{N}\bar{g}\Omega}{2\Delta} \quad .$$

The two atomic levels in the JCM are replaced by the collective ground state and the state with exactly one Rydberg excitation

$$|\mathrm{G}^{(N)}\rangle = |\mathrm{g}_1, \mathrm{g}_2, \ldots, \mathrm{g}_N\rangle$$
$$|\mathrm{E}^{(N)}\rangle = \frac{1}{\sqrt{N}} \sum_{i=1}^{N} \frac{g(\mathbf{r}_i)}{\bar{g}} |\mathrm{g}_1, \mathrm{g}_2, \ldots, \mathrm{g}_{i-1}, \mathrm{R}_i, \mathrm{g}_{i+1}, \ldots, \mathrm{g}_N\rangle$$

This three-level scheme allows us to study the $\chi^{(3)}$ non-linearity of the system. The predicted non-linearity is very strong but also saturates very quickly: if the cavity is driven by a strong beam, the Rydberg level would be significantly populated. In this situation, the additional energy shift due to the Rydberg blockade effect can shift the Rydberg level out of resonance with the coupling beam. The strong coupling beam hence no longer couples the intermediate state to any Rydberg state and the system effectively falls back to a Tavis-Cummings model (see Fig. 2.4) [16].

In our experiment, we use ^{87}Rb and the states of interest are

$$\begin{aligned} |\mathrm{G}\rangle &= |5\,^2S_{1/2}, F = 2, m_F = 2\rangle \\ |\mathrm{I}\rangle &= |5\,^2P_{3/2}, F' = 3, m_{F'} = 3\rangle \\ |\mathrm{E}\rangle &= |nS_{1/2}, F'' = 2, m_{F''} = 2\rangle \quad \text{with } n \approx 50 - 52. \end{aligned}$$

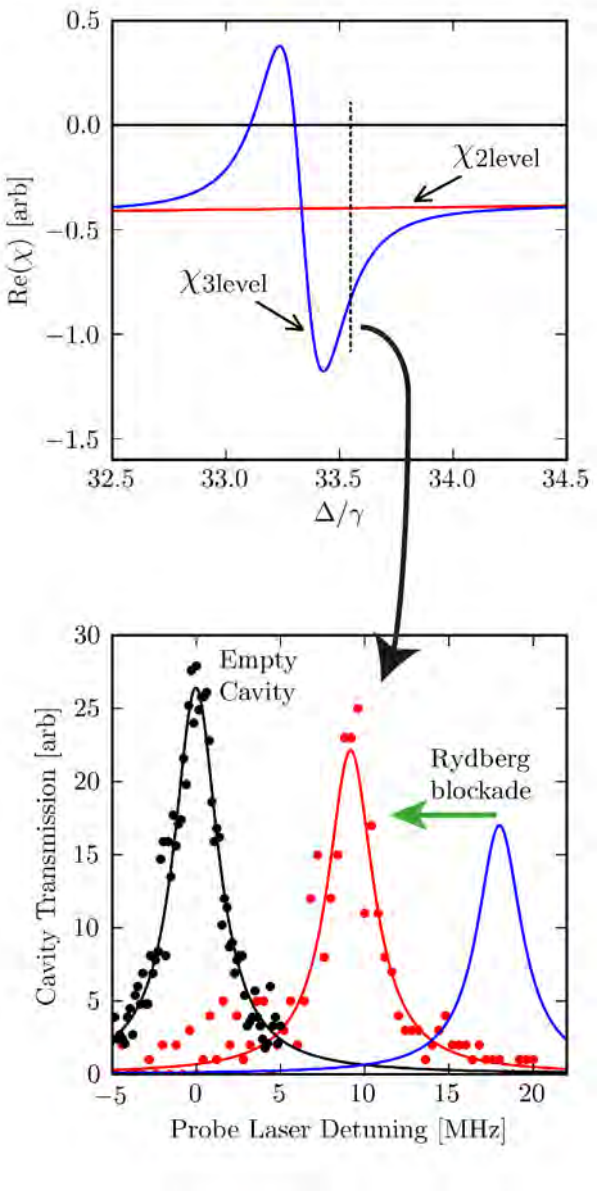

Figure 2.4: Plots from [16].
Top: the phase shifts induced by a two-level coupling and a three-level coupling as a function of cavity detuning. The black dashed line indicates the cavity detuning during the cavity probing process.
Bottom: the cavity transmission as a function of probe detuning. In black, the empty cavity transmission; in red, the dispersively shifted cavity transmission due to the two-level coupling; in blue, the dispersively shifted cavity transmission due to the three-level coupling. We can see that when the ensemble is Rydberg-blockaded the three-level system falls back to a two-level system.

Chapter 3

Experimental Setup

In this chapter, the tools required in the experiment will be discussed in detail. We start with the construction of the moderate finesse optical cavity, followed by the vacuum system used, and finally the individual setup of the major laser systems.

3.1 Optical Cavity

The optical cavity serves to amplify the coupling between the atoms and the electromagnetic field. For this, the cavity mirrors need to have high reflectivity and low loss to enhance the lifetime of photons in the cavity. Our optical cavity is constructed with two concave mirrors with a broadband high reflectivity coating provided by ATFilms. The mirrors' coating is specified to have transmissive loss of $\mathcal{T} \approx 0.25\%$ and absorptive loss $\mathcal{A} < 4$ ppm for wavelengths ranging from 650 nm to 1 μm. The reflectivity of the mirrors' coating depends slightly on the wavelength, therefore the finesse of the cavity is expected to be different for different wavelengths.

The specifications of our optical cavity at the relevant wavelengths are summarized in the Table 3.1.

Description	Value	Unit
Length	6.3	cm
Radius of curvature of cavity mirrors	10	cm
Diameter of cavity mirrors	1.27	cm
Waist at 780 nm	107	μm
Waist at 808 nm	109	μm
Finesse at 780 nm	1200	
Finesse at 808 nm	3000	

Table 3.1: Specifications of optical cavity.

As can be seen in Table 3.1, our cavity is long and of moderate finesse. This design allows us to create the cold atom cloud directly within the cavity, avoiding the complications of transporting the cold atoms.

3.1.1 Cavity Length Actuator and Ground Shielding

The length of the cavity is fine-tuned using high voltage shear-mode Lead Zirconate Titanate (PZT) piezoelectric transducers. The PZT is first attached to a piece of Macor with TorrSeal and some silver epoxy. The TorrSeal serves to fix the PZT to the Macor base, while the silver epoxy serves to make electrical contact. Some extra silver epoxy is applied to make a lead that extends out of the PZT bottom as detailed in Fig. 3.1

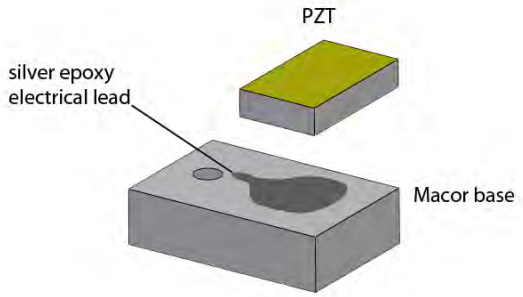

Figure 3.1: Mounting of PZT onto the Macor base.

Because Rydberg atoms have high polarizability, they are very sensitive to stray electric field gradients. To shield the atoms from the electric field created by the high voltage applied on the PZT's, the PZT's are surrounded by grounding shields made of aluminium. High voltage is applied onto the bottom of the PZT through the electrical lead created

using silver epoxy, and the top is grounded. The cavity mirrors reside in two aluminium ground shields mounted directly onto the PZT with silver epoxy. Another advantage in doing so is that we could keep the mirrors from the line-of-sight of the Rubidium dispenser, which helps to prevent the mirrors from being coated with Rubidium. A small tapped hole on the side of the mirror shields allows it to be grounded via a gold ribbon.

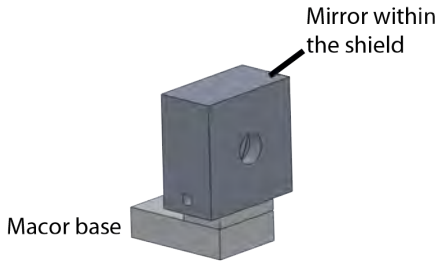

(a) Shielded mirror.

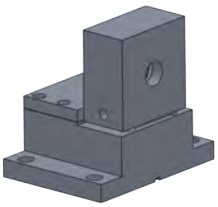

(b) Full ground shield.

3.2 Vacuum System

The vacuum system used for this experiment consists of the following standard components:

- Ion pump
- UHV vacuum valve for attachment and detachment of molecular turbo pump
- Titanium Sublimation Pump (TSP), necessary to reach low pressure
- 6.0" Spherical Octagon vacuum chamber, the experiment chamber
- An 8-pin vacuum wire feedthrough

In order to reach ultra high vacuum (pressure $< 10^{-9}$ Torr), it is essential to use high vacuum compatible components during the construction. For instance, normal adhesive would outgas too much in such a low pressure environment, preventing the pressure from decreasing beyond $10^{-6} - 10^{-8}$ Torr. Moreover, it is also necessary for the system to undergo the baking process whereby the outgassing of the contaminants that entered the chamber (e.g. water vapour, oil particle etc.) during the construction process is sped up enormously and pumped out via the molecular turbo pump. Therefore, we also require that the construction materials are able to withstand high temperature. In general, the

higher the temperature at which we bake the system, the lower the ultimately achievable pressure. The limit of the baking temperature is mainly set by the different materials used. For instance, in our experiment, we observed the TorrSeal vacuum epoxy used to attach the different components turned brownish and brittle when baked at $\sim 120°$C. Therefore, our current system was baked at $\sim 100°$C.

To minimize the outgassing, we use only Kapton coated copper wires, high vacuum epoxy such as Varian's TorrSeal, and silver infused epoxy EPO-TEK H20E provided by Epoxy Technology. With the molecular turbo pump, we could reach a pressure on the order of 10^{-7} Torr after baking. With the valve closed and after running the TSP, the ion pump pulls the pressure further down to 10^{-11} Torr.

3.2.1 Vibrational Isolation Stack

In order to improve the passive stability of the system, the cavity is mounted onto an isolation stack consists of a 0.5 kg stainless steel cylinder and three pieces of Viton rubber as can be see in Fig. 3.2. The rubber serves to vibrationally isolate the cavity from the environment, while the stainless steel cylinder increases the mass of the assembly to damp out any oscillation. The cylinder also lowers the center of gravity of the assembly, stabilizing it on the rubber feet.

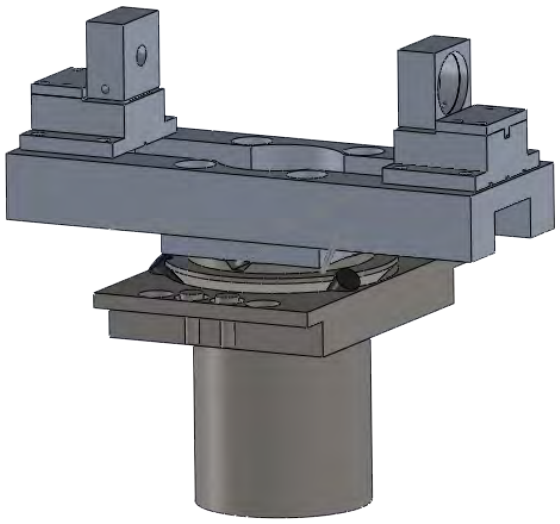

Figure 3.2: Complete cavity setup together with the isolation stack.

3.3 Laser Systems

In this experiment, several laser systems are required for the following purposes:

- Magneto-Optical Trap (MOT) lasers for the cold atom cloud preparation
- A far-detuned Dipole Trap to trap the cooled atomic ensemble without scattering
- A 780 nm cavity probe beam to measure the cavity dispersive shift due to the atom-cavity mode interaction
- A 480 nm strong coupling beam for the two-photon transition from the atomic ground state to a Rydberg state

This section is devoted to detailing the construction of each of these systems.

3.3.1 Magneto-Optical Trap (MOT) Laser

Our MOT beams consist of three narrow linewidth (relative to the atomic cooling transition) laser beams propagating in the three orthogonal directions with balanced power of more than 20 mW. Therefore, a total of 60 mW is required, without taking into account the loss due to optical fibre couplings and other optical elements. We opted to use a Tapered Amplifier (TA) seeded by a Master laser (hereon denoted as Master 1), which is a standard grating stabilized External Cavity Diode Laser (ECDL) in the Littrow configuration. This configuration allows us to select the frequency range of interest and fine-tune the frequencies by changing the grating angle and the external cavity length.

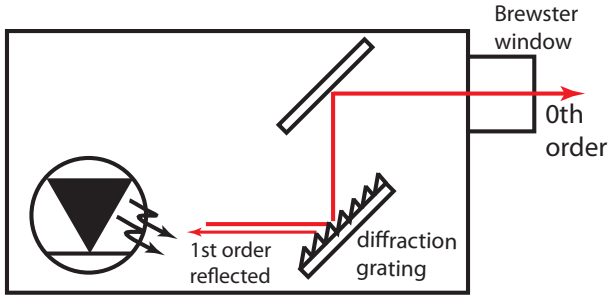

Figure 3.3: External Cavity Diode Laser (ECDL) in the Littrow configuration.

To pin down the frequency of the laser, we use an offset phase-locking scheme to lock Master 1 to another laser (Master 2) of fixed frequency with an offset given by a voltage-controlled oscillator (VCO) as shown in Fig. 3.4. When both the lasers are locked, the

frequencies should satisfy the frequency difference relation

$$|f_{\text{Master 1}} - f_{\text{Master 2}}| = f_{\text{VCO}}$$

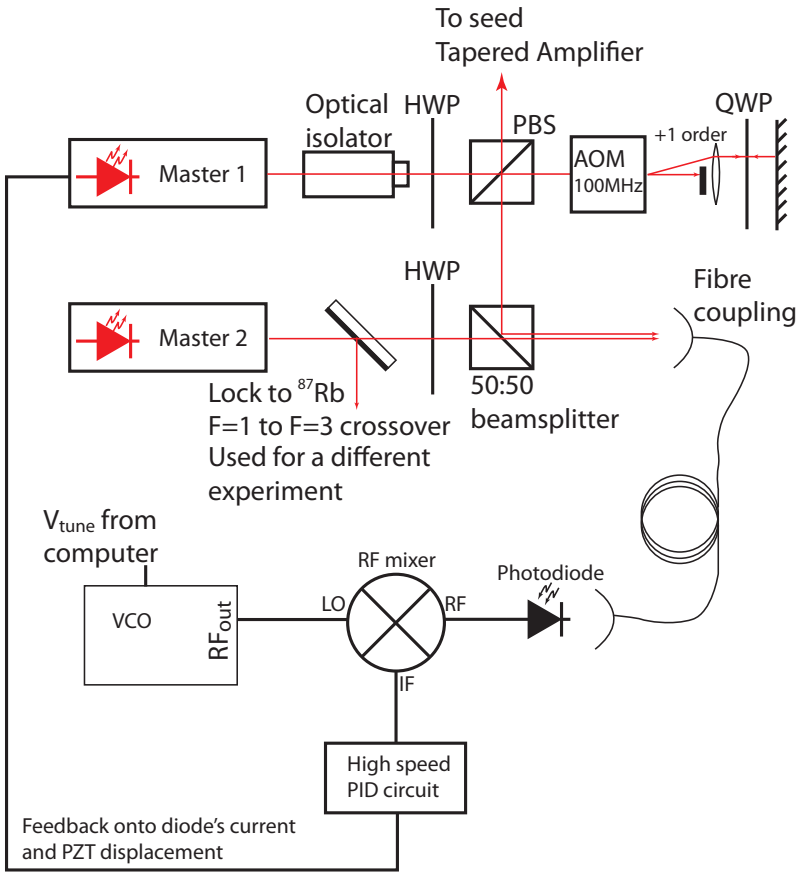

Figure 3.4: Schematic of phase-locking scheme. HWP = Half waveplate, PBS = Polarization Beam Splitter, VCO = Voltage Controlled Oscillator, AOM = Acouto-Optical Modulator. Fibre coupling the two beams simplifies the alignment procedure.

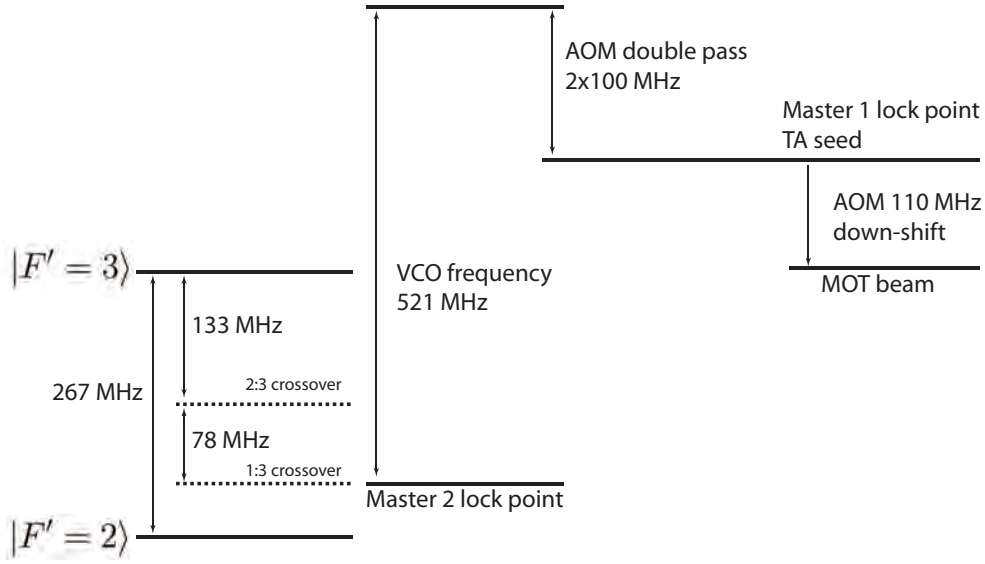

Figure 3.5: Different frequency shifts and lock points of Master 1 and Master 2. The two atomic states are the hyperfine states of interest of ^{87}Rb. This diagram is drawn with a VCO frequency of 521 MHz, which results in the MOT beam being at the same frequency as the $|F=2\rangle \longrightarrow |F'=3\rangle$ transition. By changing the VCO frequency, the MOT beam can be shifted to anywhere between the $|F=2\rangle \longrightarrow |F'=3\rangle$ resonance and the $|F=2\rangle \longrightarrow |F'=2\rangle$ resonance.

As the VCO's frequency is changed, the current feedback maintains the phase lock between the lasers while the PZT feedback moves the external cavity to a new position that satisfies the frequency difference relation. Therefore, this offset phase-locking scheme allows us to tune the frequency of Master 1 continuously by simply changing the frequency of the VCO. This is very useful when the MOT beams are used subsequently to perform the sub-Doppler cooling where the laser beams need to be swept to further red-detunings from the atomic transition. This setup also allows us to use the same laser for resonant imaging on the $|F=2, m_F=2\rangle \longrightarrow |F'=3, m_{F'}=3\rangle$ transition and optical pumping on the $|F=2, m_F=2\rangle \longrightarrow |F'=2, m_{F'}=2\rangle$ transition.

The verification of a successful phase lock can be done by measuring the beat note between Master 1 and Master 2. This measurement shows that we achieve a phase-locking bandwidth of $\sim$1.5 MHz.

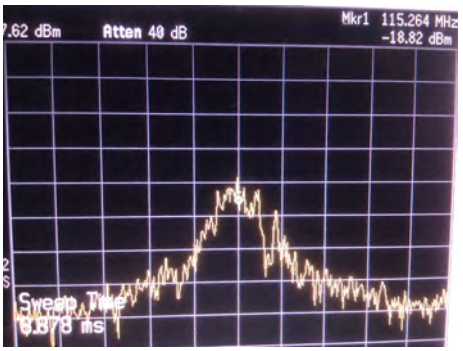

(a) Beat note before the phase lock is engaged.

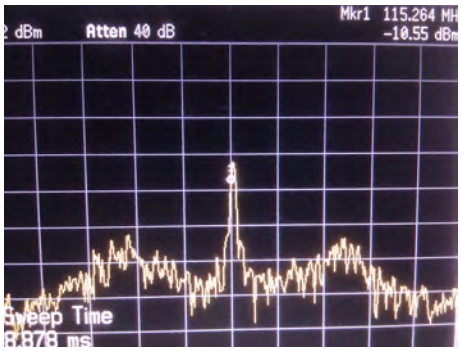

(b) Beat note with the phase lock engaged

Figure 3.6: Traces of the spectrum analyzer showing the comparison before and after the phase lock is engaged. The horizontal scale is 0.6 MHz/div and the vertical scale is 10 dB/div. The spectrum analyser measures the spectral component of the beat note between Master 1 and a frequency-shifted copy of Master 2 by an Acousto-Optical Modulator of frequency 115 MHz. The phase noise of Master 1 is clearly suppressed when the lock is engaged.

With a seed power of 8 mW, it is sufficient to saturate the gain of the TA. The spectral quality of the TA output is checked by performing a saturated absorption spectroscopy and observing that the Amplified Spontaneous Emission (ASE) background is relatively suppressed when the seed power is increased. An Acousto-Optical Modulator (AOM) at 110 MHz is used as a high-speed switch to control the MOT beams' power. A mechanical shutter (not in the diagram) is also used to block any residual light from the TA even when the AOM is toggled off to increase the subsequent lifetime of atoms in the dipole trap. A three-way fibre splitter is used before the vacuum chamber to split the beam into three equal portions for the MOT. At a current of 1.7A through the TA, we achieve 45-50 mW at each arm of the fibre splitter.

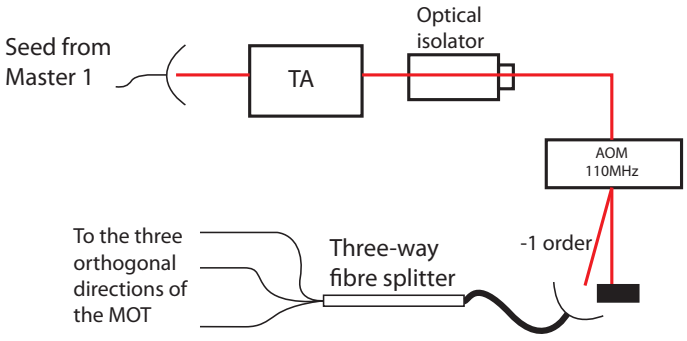

Figure 3.7: Tapered Amplifier's setup.

3.3.2 808 nm Dipole Trap Laser

The 808 nm far-detuned dipole trap beam is generated by an ECDL in the Littrow configuration (Fig. 3.3). The frequency of the dipole beam typically need not be referenced to any exact atomic transition as it is very far-detuned. However, in our setup, this dipole beam will also be used to stabilize our experimental cavity. The cavity needs to be transmissive for both the 808 nm dipole beam and the 780 nm probe beam, therefore the laser requires a stable and tunable frequency for us to adjust the cavity's transmission window. We lock the dipole beam to a reference cavity using the Pound-Drever-Hall (PDH) method with a tunable offset achieved using an EOspace device. The EOspace device is a low-loss $LiNbO_3$-based fibre device for wideband (10 GHz) phase-modulation at low drive voltages. This phase modulation creates sidebands on the laser's optical frequency at the RF drive frequency. Locking either of the sidebands to the reference cavity allows us to shift the carier frequency by tuning the RF frequency sent to the EOspace device. The experiment cavity is then stabilized to the 808 nm laser, hence the length of the cavity is tuned by changing the dipole beam's frequency. Thus, having the freedom to shift the laser's frequency allows us to ensure the overlap of the transmission window for both the cavity probe beam and the dipole trap beam. It also allows us to choose our cavity detuning with respect to the atomic transition.

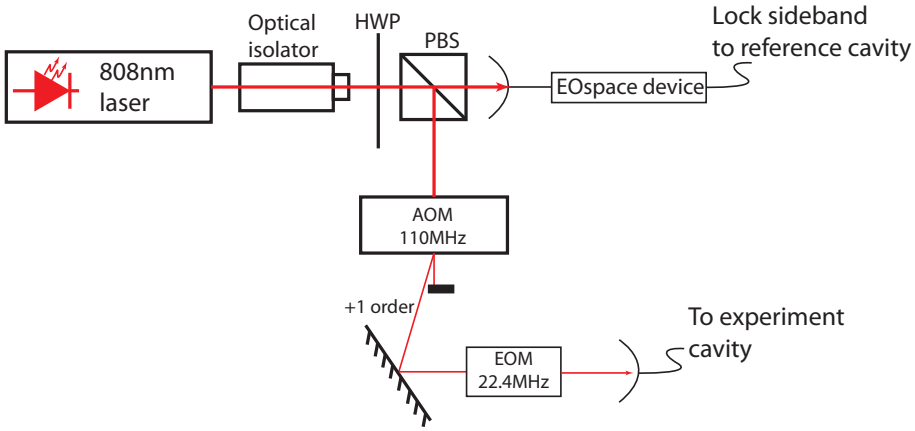

Figure 3.8: Schematic diagram of 808 nm laser setup.

Before injecting into the fibre that brings the laser to the experiment, a homebuilt Electro-Optical Modulator (EOM) is used to create 22.4 MHz sidebands that will be used for the PDH stabilization of the experimental cavity. In this configuration, we obtain an output power of 10-11 mW before it enters the experiment cavity.

3.3.3 780 nm Cavity Probing Laser

The 780 nm cavity probe laser is also an ECDL in the Littrow configuration. To have a narrower linewidth and to gain in stability, we opted for a longer extended cavity to reduce the sensitivity of the laser to current noise [20]. The extended cavity length is ≈13 cm. The expected linewidth is on the order of 1-10 kHz.

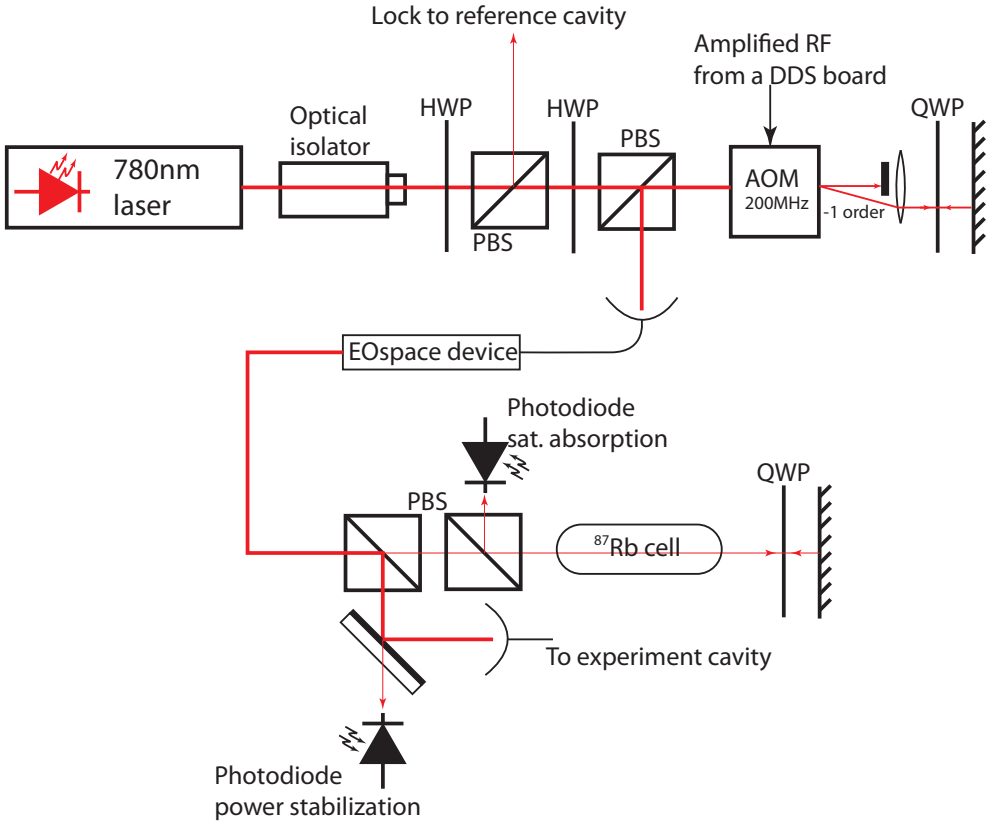

Figure 3.9: Schematic diagram of 780 nm cavity probe beam setup. DDS = Direct Digital Synthesizer.

For the purpose of probing the cavity, we first lock the laser to a reference cavity and use only one of the sidebands generated using an EOspace device as the cavity probe. The carrier of the laser is locked to a frequency $\gtrsim 700$ MHz above the $|F = 2\rangle \longrightarrow |F' = 3\rangle$ transition. It is then double pass down-shifted by a 200 MHz AOM. The EOspace device is then used to generate two ~ 300 MHz sidebands of which one will be close to the atomic transition. An ^{87}Rb cell is used at the output of the EOspace device to perform the saturated absorption spectroscopy, and appropriate corrections are applied onto the EOspace frequency to maintain the probe beam's relative frequency to the atomic transition.

The AOM RF frequency is derived from a Direct Digital Synthesizer (DDS) board that is based on the AD9958 chip from Analogue Devices. To perform a fast frequency sweep during the cavity probing, we use the linear sweep function of the DDS board.

3.3.4 Frequency-Doubled 480 nm Coupling Laser

The 480 nm laser is required to achieve the two photon coupling between the $|5\,^2S_{1/2}, F = 2, m_F = 2\rangle$, and the $n\,S_{1/2}$ Rydberg state via the intermediate state $|5\,^2P_{3/2}, F' = 3, m_{F'} = 3\rangle$. This source is generated by frequency doubling a high-power 960 nm beam using a periodically-poled KTP non-linear crystal.

Initially, the 960 nm beam was constructed as an ECDL in the Littrow configuration using a high-power 980 nm diode. This setup involved water cooling the laser housing and cooling down the diode to $\sim -5°$C in order to pull the diode's gain profile to 960 nm. We soon realized that the diode got very unstable at a current of > 200 mA (maximum current rating is 450 mA) and the laser tended to mode-hop easily. Moreover, it was very inconvenient to tune the grating angle because a dry atmosphere had to be maintained at all times to prevent condensation on the diode. Therefore, we resorted to a new Master/Slave injection lock configuration achieved using a low-power 960 nm AntiReflective-coated Master seed laser diode and the same high-power Slave laser diode. It is still necessary to cool the Slave diode to $\sim 5°$C however the mechanical tuning (grating and mirror) is only required for the AR-coated diode which can be done at the room temperature. With this setup, the diffraction grating is no longer required for the Slave diode and we achieve a higher output power. The AR-coated Master diode uses an extended housing of ~ 7 cm and an EOspace device is used for the fine-tuning of the seeding frequency.

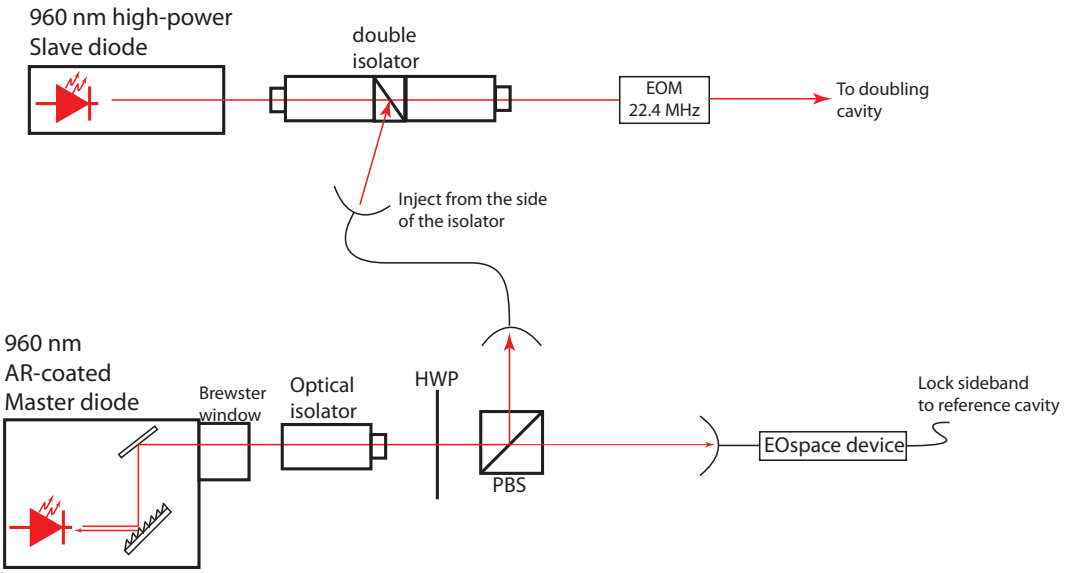

Figure 3.10: Schematic diagram of the injection locking setup using an AR-coated Master diode and a high-power Slave diode.

25% of the $\sim 9.6\,\mathrm{mW}$ seed power is mode-matched to the Slave diode. Considering the coupling loss through the double isolator, some fraction of 2.5 mW is seeding the Slave diode. This is sufficient to force the Slave diode to lase at the seed frequency at a current of $\gtrsim 300\,\mathrm{mA}$.

To achieve efficient frequency doubling, we constructed a bowtie doubling cavity with a similar design as in [21]. The use of a doubling cavity enhances the circulating power through the doubling crystal, resulting in a much higher overall conversion efficiency compared to single pass. The single pass efficiency of the crystal is η =1.2%/W at the optimal waist of 30 μm. At this waist, we observed that the doubling efficiency dropped over time and this is attributed to the photo-refractive damage of the crystal. In order to avoid the photo-refractive damage, we decided to double the waist at the crystal and the input power. In doing so, the incident intensity at the crystal is halved, but the single pass efficiency dropped to 0.3%/W as it is inversely proportional to the square of the waist.

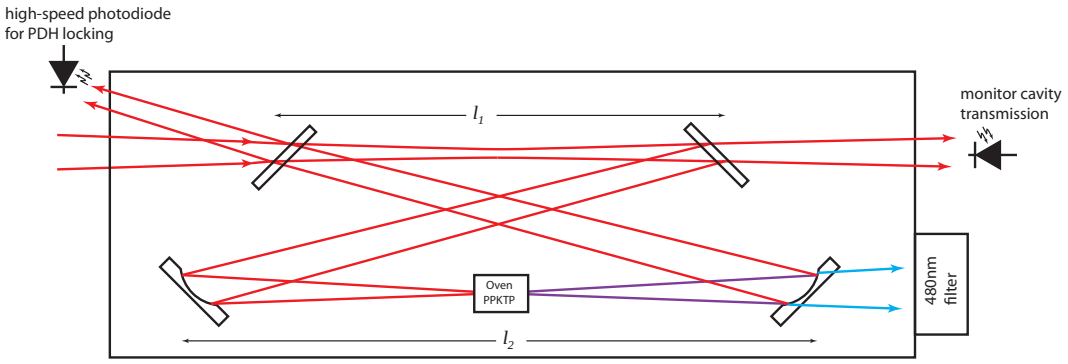

Figure 3.11: Bowtie doubling cavity schematic diagram.

Description	Value	Unit
ℓ_1	72	mm
ℓ_2 (physical path)	113.23	mm
Radius of curvature of concave mirrors	100	mm
Length of crystal	10	mm
Folding angle	15	degree
Optical coupler's reflectivity @ 960 nm	0.99	
Horizontal waist at short arm	169	μm
Vertical waist at short arm	201	μm
Horizontal waist at crystal	65	μm
Vertical waist at crystal	67	μm

Table 3.2: Specifications of the 960 nm doubling cavity. The cavity geometry is designed to have a circular waist at the crystal, but this requires an elliptical beam in the short arm [22].

The temperature of the crystal is controlled with a homebuilt temperature controller, actuating on a peltier device. The temperature tuning is crucial as the period of the poling has to match the wavelength of the laser in order to achieve efficient second harmonic generation; by changing the temperature, the length of the crystal is modified, effectively modifying the poling period. With the cavity locked to the the laser, and an input 960 nm power of 170 mW, we achieve an overall conversion efficiency of $\sim$45%, taking into account the $\sim$80% coupling into the cavity due to impedance mismatch. The output power of 480 nm beam is 40-50 mW.

Chapter 4

Cold Atom Preparation

4.1 Magneto-Optical Trap (MOT)

Our MOT setup consists of three pairs of counter-propagating laser beams with opposite circular polarization and two circular copper coils in the anti-Helmholtz configuration (hereafter referred to as the MOT coils). The laser source is achieved with the a tapered amplifier as detailed in Sec. 3.3.1. There is ≈ 40 mW in each beam, with a beam waist of 25.4 mm.

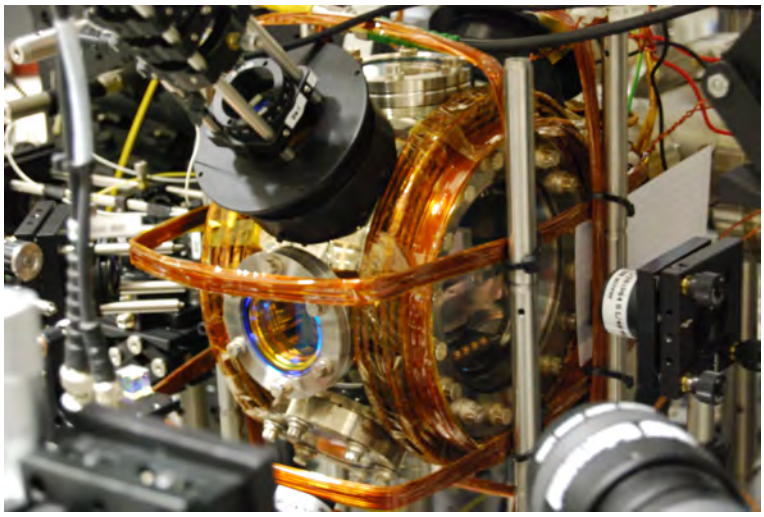

Figure 4.1: Experiment chamber with MOT coils and offset coils mounted.

The $5^2S_{1/2}|F = 2\rangle \longrightarrow 5^2P_{3/2}|F' = 3\rangle$ transition is used as the cooling transition. The MOT beams are 18 MHz red-detuned from this transition. During the cooling,

off-resonance scattering could bring the atoms into the $F = 1$ ground state that is not addressed by the MOT beams. A repump beam of ∼5 mW locked to the $5^2S_{1/2}|F = 1\rangle \longrightarrow 5^2P_{3/2}|F' = 2\rangle$ transition is then used to pump the atoms back into the cooling cycle. The final temperature of a MOT is on the order of the linewidth of the cooling transition,

$$T \sim \frac{\hbar\Gamma}{k_B} = 300\,\mu\text{K}.$$

Additionally, as can be seen from Fig. 4.1, offset coils are mounted around the chamber in the Helmholtz configuration to generate fixed uniform magnetic fields in the three orthogonal directions to displace the centre of the MOT. This is necessary in order to move the MOT into the cavity, and they will subsequently be used in optical pumping to define a quantization axis.

4.2 Sub-Doppler Cooling

Our MOT reaches a steady state atom number of ~ 12 millions in five seconds, the MOT beams' detuning are then further increased to -220 MHz and its power is reduced for the sub-Doppler cooling [23, 24]. In our setup, the temperature at the end of the sub-Doppler cooling process is around $50\,\mu$K.

4.3 Cavity Assisted Dipole Trap

An electric dipole is induced in the atom when it is placed in a strong electric field. An optical dipole trap basically exploits the force exerted on the dipole by the spatial gradient of the laser's electric field amplitude. For a laser red-detuned from the atomic frequency, the atoms are attracted to the most intense part of the beam. We additionally rely on the cavity to amplify the electric field, creating a trap sufficiently deep directly in the cavity mode.

However, the cavity enhancement effect happens only when the laser is resonant with the cavity. The cavity is therefore locked to our 808 nm laser using the Pound-Drever-Hall method, stabilizing its length.

It turns out that we are not able to completely suppress the vibrational noise using a

servo-control system actuating on the PZT attached to the cavity mirrors due to the low resonance frequency of the PZT used in the experiment ($\sim$ 2 kHz). Fluctuation can be seen on the cavity transmission corresponding to the fluctuation of the intracavity circulating power. This will compromise the stability of the dipole trap. Therefore, we implemented an alternative AC locking scheme which effectively locks the 808 nm laser's frequency onto our cavity to suppress the residual fast fluctuations ($\gtrsim$ 1 MHz).

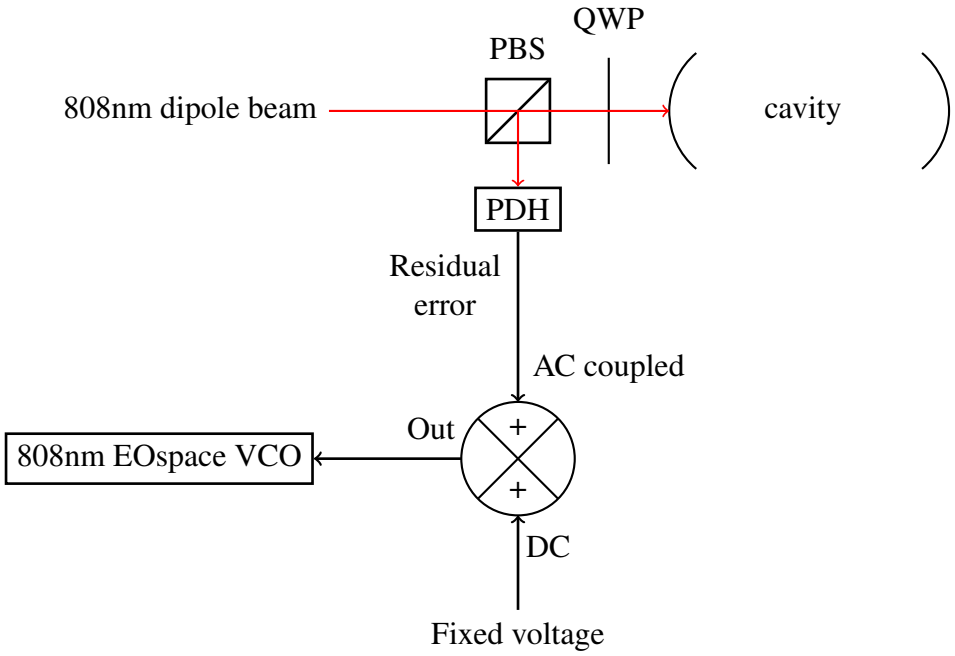

Figure 4.2: AC locking scheme

As shown in Fig. 4.2, the residual PDH error signal from the cavity stabilization circuit is AC coupled into the tuning voltage of the VCO driving the 808 nm EOspace device. The RF sidebands of the 808 nm laser are thus shifted. With one of the laser sidebands actively stabilized to the reference cavity (ref. Sec. 3.3.2), this effectively shifts the laser's carrier frequency. With the high locking bandwidth of the laser ($\sim$ 2 MHz), the residual error is fully suppressed.

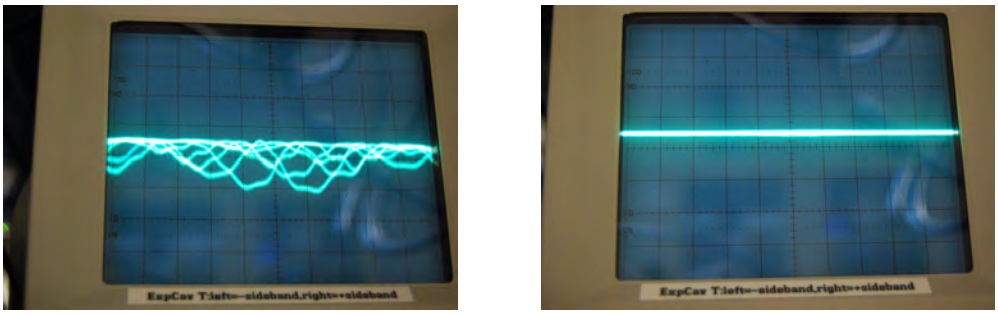

(a) Before the AC lock is engaged. (b) With AC lock engaged.

Figure 4.3: Oscilloscope traces of the cavity transmission for the 808 nm laser. They show the effectiveness of the AC locking scheme.

As shown in Fig. 4.3, with the AC locking scheme in place, we achieved the desired stability. The overall cavity transmission for 808 nm is $\sim 30\%$. With an input power of ~ 10 mW, and single cavity mirror transmissive loss of $\mathcal{T}_{808} = 0.001$, we infer a 3 W intracavity circulating power. The trap depth differs for different Zeeman substates because the beam enters the cavity with circular polarization and induces Stark shifts that depend on the m_F quantum number.

m_F	Stark shift (MHz)	Trap depth (μK)
-2	-23.91	1147.37
-1	-21.29	1021.55
0	-18.66	895.72
1	-16.04	769.90
2	-13.42	644.08

Table 4.1: Stark shift and trap depth of different m_F states of the ground level.

The trap is imaged by fluorescence imaging using the MOT beams 100 ms after the MOT is turned off.

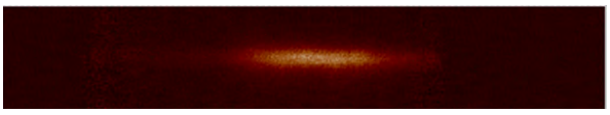

Figure 4.4: Image of atoms in the dipole trap. Atoms are trapped along the cavity mode as can be seen from the elongated trap shape.

Nevertheless, this AC locking scheme has introduced extra complications. Although the 808 nm laser always remains resonant with the cavity, the cavity is in fact jittering, what

we achieved was transferring this jitter onto the laser. This means the same amount of jitter needs to be transferred onto all other lasers that will enter the cavity, in particular the 780 nm probe laser. We employ a single-sideband upconversion scheme using a DDS chip to achieve this frequency feedforward. As it is not crucial to the flow of the report, the details of this scheme will be included the appendix A.

Chapter 5

Cavity Probing

In this chapter, we will describe the procedure of probing the cavity and report the preliminary result on the dispersive shift measurement. This number allows us to infer the number of atoms trapped in the intra-cavity dipole trap.

During each cycle of the experiment, the MOT is first loaded for 5 s. Then, the detuning of the MOT beams is increased while the power is lowered for sub-Doppler cooling. At the end of the sub-Doppler cooling process, the repump beam is shuttered first before the MOT beams in order to pump the atoms into the $F = 1$ ground state to avoid hyperfine-changing collisions that can lead to loss of atoms in the dipole trap. The current in offset magnetic coils are set such that the spatial position of the MOT is overlapped with the dipole trap to obtain optimal loading. We wait for 100 ms for the MOT cloud to diffuse before we turn on the probe beam, trigger the Single Photon Counting Module (SPCM) and start the frequency sweep. It is also necessary to turn the repump beam back on during the cavity probing phase to pump the atoms back into the $F = 2$ level in order for them to interact with the probe beam.

The cavity is tuned such that the cavity detuning with respect to the $|F = 2\rangle \longrightarrow |F' = 3\rangle$ transition is $\Delta = 2\pi \times 100\,\text{MHz}$. The power of the probe beam is set such that on resonance with an empty cavity, there is on average $\bar{n} \approx 0.4$ photons in the cavity.

5.1 Preliminary Result

At the current stage of the experiment, the dispersive shift due to the coupling between the cavity and the atomic transition $|F = 2\rangle \rightarrow |F' = 3\rangle$ is measured.

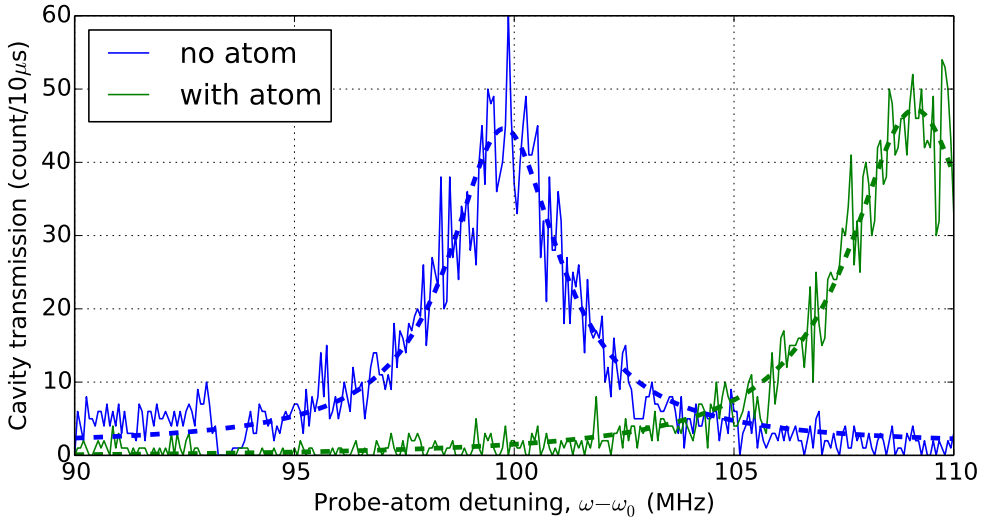

Figure 5.1: Dispersive shift measurement with Δ_c =100 MHz, the transmission is shifted by 9 MHz in the presence of atoms.

This signal can also be used to optimize the dipole trap loading: the more atoms load into the dipole trap, the greater the dispersive shift as it scales linearly with N.

5.2 Analysis and Discussion

The mode volume of the cavity and the single photon field amplitude can be calculated [25] with the cavity parameters in Sec. 3.1 to be

$$\begin{aligned} V_m &= \frac{1}{4}\pi w_0 L^2 \\ &= 5.56 \times 10^{-10}\ \mathrm{m}^3 \quad , \end{aligned} \tag{5.1a}$$

$$\begin{aligned} \mathcal{E} &= \sqrt{\frac{\hbar\omega_L}{2\epsilon_0 V_m}} \\ &= 5.09\ \mathrm{Vm}^{-1} \quad . \end{aligned} \tag{5.1b}$$

For the $|F = 2, m_F = 2\rangle \longrightarrow |F' = 3, m_{F'} = 3\rangle$ transition probed using a σ^+ beam, the estimated g at a maximum field point is

$$\begin{aligned} g_{\text{max}} &= \frac{|d|\mathcal{E}}{\hbar} \\ &= 2\pi \times 195\,\text{kHz} \end{aligned} \tag{5.2}$$

using the dipole moment of the $|F = 2, m_F = 2\rangle \longrightarrow |F' = 3, m_{F'} = 3\rangle$ cycling transition in [26]. This is the strongest possible coupling between the $F = 2$ and $F' = 3$ manifolds. To take into account the spatial dependence of the coupling strength, we consider the lattice spacing of the dipole trap and the probe field.

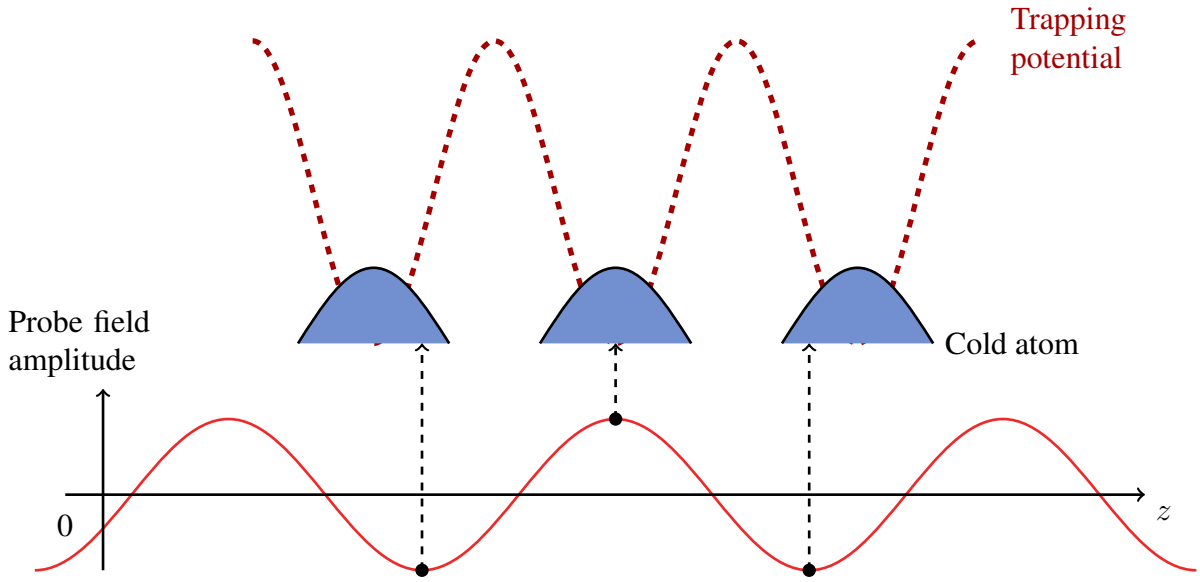

Figure 5.2: The probe field dephases relative to the trapping potential from site to site.

As shown in Fig. 5.2, the dipole trapping lattice formed by the 808 nm has a lattice spacing of 404 nm, whereas the antinodes of the 780 nm probe beam standing wave are separated by 390 nm. They therefore dephase relative to each other from site to site.

Due to this dephasing process, the total effective coupling, g_{eff} is reduced by a factor of $\overline{(\cos z)} = 1/\sqrt{2}$

$$g_{\text{eff}} = \frac{g_{\text{max}}}{\sqrt{2}} = 2\pi \times 137.8\,\text{kHz} \quad .$$

In order to infer the number of trapped atoms using Eq. 2.10, the Stark shifts of different levels due to the 808 nm dipole trap beam have to be accounted for to better estimate the cavity detuning Δ.

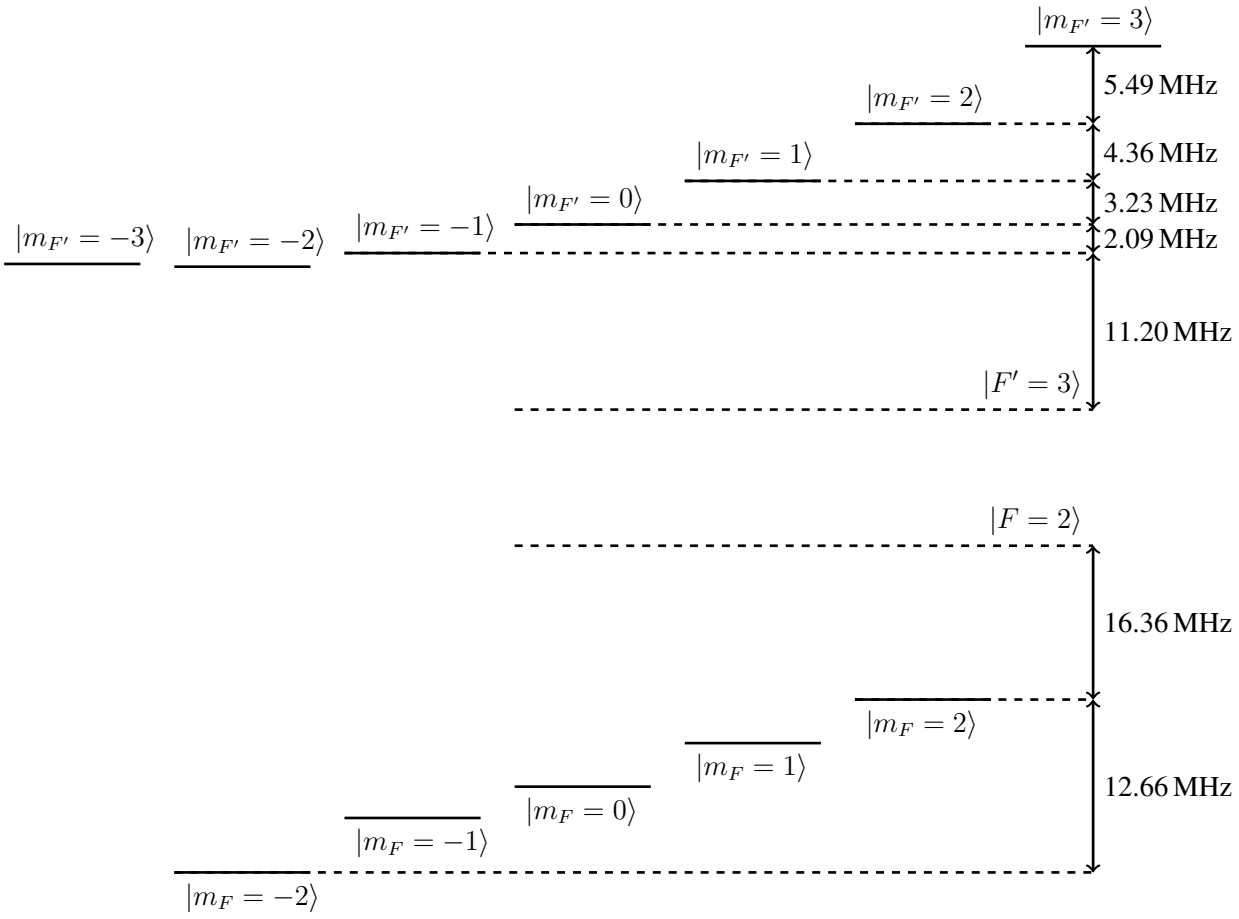

Figure 5.3: Stark-shifted Zeeman states due to the 808 nm dipole trap beam. The separation between $|F=2\rangle$ and $|F'=3\rangle$ is not drawn to scale.

Due to the fact that the ensemble is currently not optically pumped, the atoms experience different Stark shifts depending on their m_F states. We assume that when the atoms are repumped from the $F=1$ to the $F=2$ manifold, all the five Zeeman substates of $F=2$ are equally populated. An analogous calculation as in Sec. 2.1 can be carried out to compute the dispersive shift and the result is

$$\Delta_{\text{Disp}} = \frac{1}{\left(\omega_c - \frac{1}{5}\sum_{m_F=-2}^{2}\omega_{m_F}\right)^2}\frac{N}{5}g_{\text{eff}}^2\sum_{m_F=-2}^{2}\Delta_{m_F}\,c_{m_F}^2 \qquad , \tag{5.3}$$

where the coefficients $c_{m_F}^2$ are the transition strengths from the m_F Zeeman substate to the m_F+1 state of the $F'=3$ manifold [23], Δ_{m_F} and ω_{m_F} are the corrected cavity detuning and transition frequency respectively.

With this, we estimate the number of atoms in the dipole trap is $N \approx 71,000$. It should

be pointed out that the dipole trap at this stage is not optimized, the number of trapped atoms could depend very much on the trapping position and the intensity of the repump beam during the sub-Doppler cooling phase.

For a cold atomic ensemble optically pumped into the $m_F = 2$ state, the expected coupling factor and dispersive shift (with N =100,000) would be

$$\bar{g} = 2\pi \times 137\,\text{kHz} \tag{5.4a}$$

$$\Delta_{\text{Disp}} = 20\,\text{MHz} \tag{5.4b}$$

Chapter 6

Conclusion and Future Work

In summary, this year-long project consisted of the preparatory steps for an on-going experiment to explore the non-linearity in a cavity QED system in the presence of Rydberg excitations. The necessary tools including the optical cavity, the vacuum system and the required laser system were constructed. Particular emphasis is put on the engineering of the laser systems to obtain the desired stability and spectral linewidth. The basic setup is currently complete and preliminary measurements have been performed, showing that the atom-cavity coupling is strongly enhanced due to the collective coupling of the atoms to the same cavity mode.

The next step is to implement the optical pumping scheme to prepare the atoms in the correct Zeeman substates. With that, we should be in position to probe the cavity together with the coupling beam. Interesting non-trivial photon statistics accompanying the strong non-linearity in our experimental setup have also been predicted [17] and can be analyzed by measuring the photon statistics of the cavity transmission.

Appendices

Appendix A

Single-sideband Upconversion and Frequency Feedforward

In this Appendix, the complete frequency feedforward setup in Sec. 4.3 will be detailed. The necessary components for this scheme will first be introduced and the complete setup will be shown in the end of this Appendix.

A.1 Upconversion Circuit

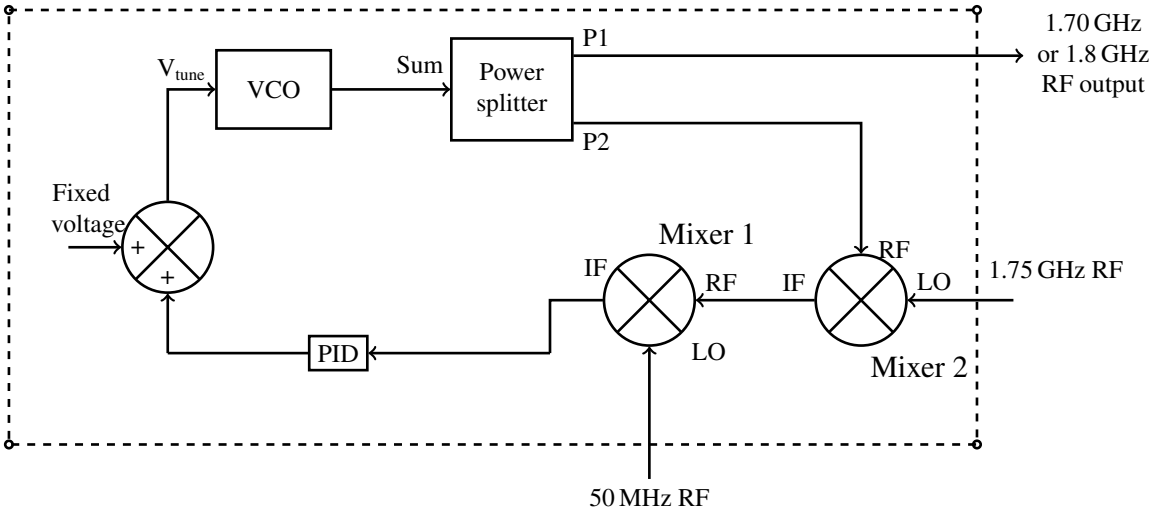

Figure A.1: Schematic drawing of the upconversion circuit.

The upconversion circuit shown in Fig.A.1 consists of phase-locked loop (PLL) that locks the VCO's output frequency to a stable oscillator. The stable oscillator is provided by a Windfreak RF Generator (at 1.75 GHz) down-shifted or up-shifted by 50 MHz achieved with an RF mixer and another 50 MHz source. By changing the fixed voltage that is sent to the VCO frequency tuning voltage port, the VCO can be locked to either the positive sideband (1.8 GHz) or the negative sideband (1.7 GHz). This circuit effectively maps any jitter of the 50 MHz source onto the VCO RF output and is a crucial component in implementing our AC-lock and frequency feedforward scheme. In our setup, the 50 MHz source is another VCO (not shown in Fig. A.1) that generates the necessary frequency correction to be applied onto the 808 nm laser to compensate for the experiment cavity jitter and the RF output is used to drive the 808 nm EOspace device.

In the following, the circuit in Fig. A.1 will be simplified to

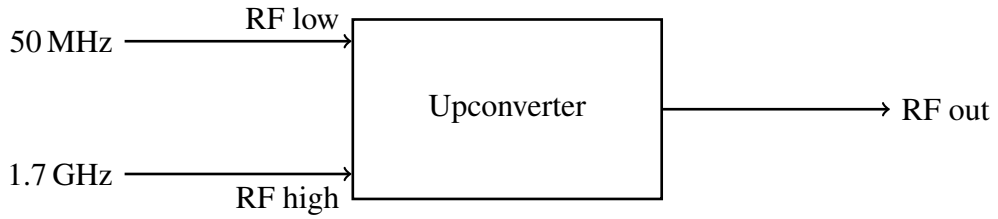

Figure A.2: Symbol of the upconversion circuit. 'RF low' and 'RF high' refers to the low frequency RF and the high frequency RF respectively.

A.2 DDS Alpha Board

The 780 nm probe laser is not locked to the experiment cavity via a PDH locking scheme, therefore the jitter of the cavity needs to be transferred onto the probe laser through the 808 nm dipole beam. For any differential change of the cavity's length δL, a frequency shift of $\delta\nu_{808}$ of the 808 nm laser is required to maintain the laser on resonance. A corresponding frequency shift of $\delta\nu_{780}$ has to be applied onto the 780 nm laser and these two frequency shifts are related by

$$\delta\nu_{780} = \frac{\lambda_{808}}{\lambda_{780}}\,\delta\nu_{808} \equiv \alpha\,\delta\nu_{808} \approx 1.036\,\delta\nu_{808}$$

where the factor α is defined as $\lambda_{808}/\lambda_{780}$.

A DDS board is configured as an 'alpha board' to achieve this transfer. This DDS alpha board does not have an on-board crystal oscillator that provides the clock frequency; it

takes in an external 50 MHz clock frequency and there is an internal PLL that clocks the DDS RF output with respect to this external clock frequency. The board is then configured to output a frequency of $\alpha \times 50\,\text{MHz} \approx 51.79\,\text{MHz}$ and the output frequency is sent to the 'RF low' port of a second upconverter that drives the 780 nm EOspace device.

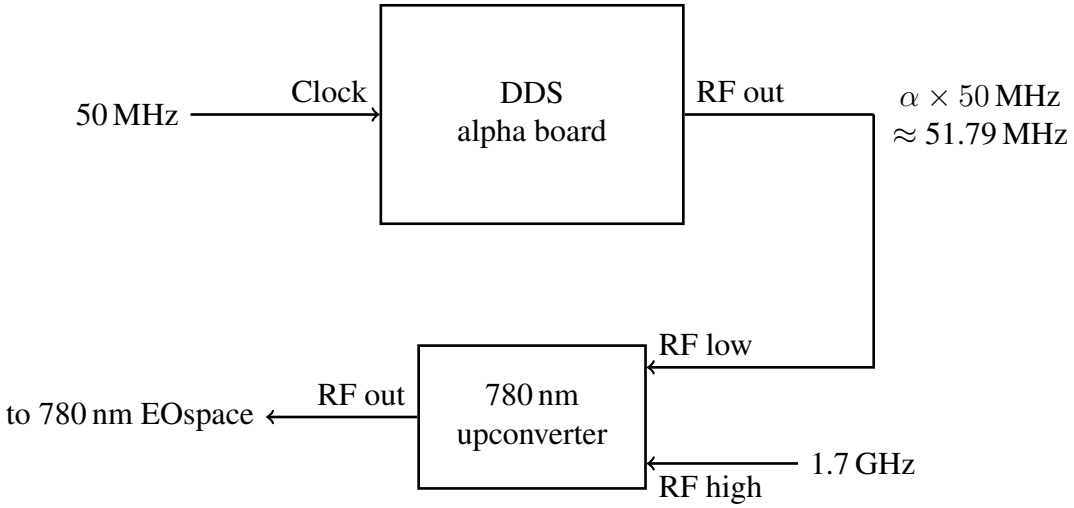

Figure A.3: DDS alpha board configuration.

A.3 Complete Frequency Feedforward Scheme

As shown in Fig. A.4, the residual fluctuation of the experiment cavity is first converted into the frequency jitter of the 50 MHz VCO. This frequency jitter is subsequently mapped onto the two lasers via the upconverters. The two Windfreak RF generators (Windfreak 2 and 3) are computer-controlled and are used to fine-tune the frequencies of the two lasers so that the 780 nm probe beam is at a fixed frequency relative to the atomic transition and the 808 nm dipole beam's cavity transmission overlaps with that of the 780 nm probe beam.

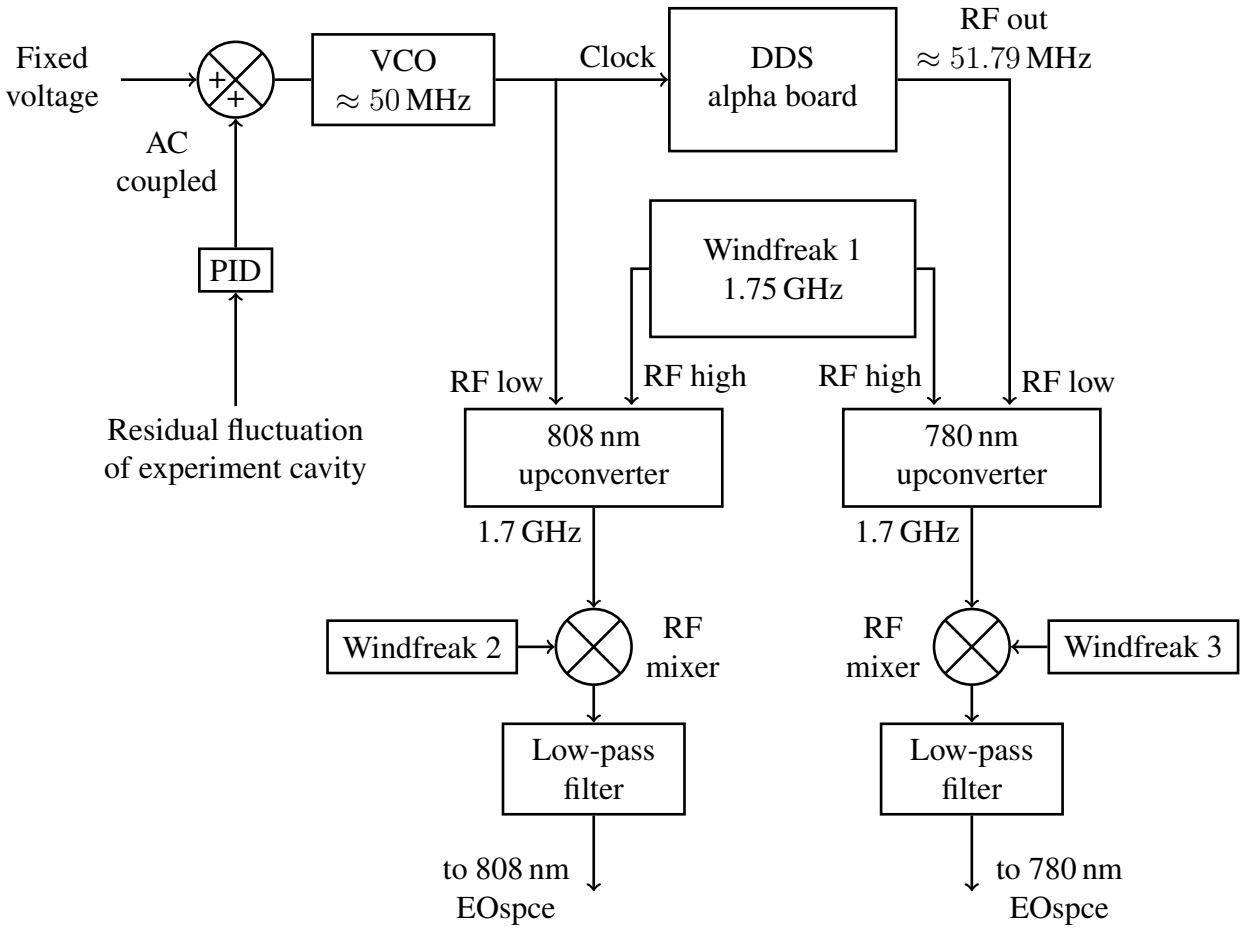

Figure A.4: Complete schematic of the frequency feedforward scheme.

Bibliography

[1] Michael A Nielsen and Isaac L Chuang. *Quantum computation and quantum information*. Cambridge university press, 2010.

[2] Shu-Shen Li, Gui-Lu Long, Feng-Shan Bai, Song-Lin Feng, and Hou-Zhi Zheng. Quantum computing. *Proceedings of the National Academy of Sciences*, 98(21):11847–11848, 2001.

[3] H_J Kimble. The quantum internet. *Nature*, 453(7198):1023–1030, 2008.

[4] Edwin T Jaynes and Frederick W Cummings. Comparison of quantum and semiclassical radiation theories with application to the beam maser. *Proceedings of the IEEE*, 51(1):89–109, 1963.

[5] Kevin M Birnbaum, Andreea Boca, Russell Miller, Allen D Boozer, Tracy E Northup, and H Jeff Kimble. Photon blockade in an optical cavity with one trapped atom. *Nature*, 436(7047):87–90, 2005.

[6] L.-M. Duan and H. J. Kimble. Scalable photonic quantum computation through cavity-assisted interactions. *Phys. Rev. Lett.*, 92:127902, Mar 2004.

[7] P Maunz, T Puppe, I Schuster, N Syassen, PWH Pinkse, and G Rempe. Normal-mode spectroscopy of a single-bound-atom–cavity system. *Physical review letters*, 94(3):033002, 2005.

[8] I Schuster, A Kubanek, A Fuhrmanek, T Puppe, PWH Pinkse, K Murr, and G Rempe. Nonlinear spectroscopy of photons bound to one atom. *Nature Physics*, 4(5):382–385, 2008.

[9] Stephan Ritter, Christian Nölleke, Carolin Hahn, Andreas Reiserer, Andreas Neuzner, Manuel Uphoff, Martin Mücke, Eden Figueroa, Joerg Bochmann, and Gerhard Rempe. An elementary quantum network of single atoms in optical cavities. *Nature*, 484(7393):195–200, 2012.

[10] Kyung Soo Choi, Hui Deng, Julien Laurat, and HJ Kimble. Mapping photonic entanglement into and out of a quantum memory. *Nature*, 452(7183):67–71, 2008.

[11] Adam T Black, James K Thompson, and Vladan Vuletić. On-demand superradiant conversion of atomic spin gratings into single photons with high efficiency. *Physical review letters*, 95(13):133601, 2005.

[12] S Sevinçli, N Henkel, C Ates, and T Pohl. Nonlocal nonlinear optics in cold rydberg gases. *Physical review letters*, 107(15):153001, 2011.

[13] Thibault Peyronel, Ofer Firstenberg, Qi-Yu Liang, Sebastian Hofferberth, Alexey V Gorshkov, Thomas Pohl, Mikhail D Lukin, and Vladan Vuletić. Quantum nonlinear optics with single photons enabled by strongly interacting atoms. *Nature*, 488(7409):57–60, 2012.

[14] Ofer Firstenberg, Thibault Peyronel, Qi-Yu Liang, Alexey V Gorshkov, Mikhail D Lukin, and Vladan Vuletić. Attractive photons in a quantum nonlinear medium. *Nature*, 2013.

[15] Christine Guerlin, Etienne Brion, Tilman Esslinger, and Klaus Mølmer. Cavity quantum electrodynamics with a rydberg-blocked atomic ensemble. *Physical Review A*, 82(5):053832, 2010.

[16] Valentina Parigi, Erwan Bimbard, Jovica Stanojevic, Andrew J. Hilliard, Florence Nogrette, Rosa Tualle-Brouri, Alexei Ourjoumtsev, and Philippe Grangier. Observation and measurement of interaction-induced dispersive optical nonlinearities in an ensemble of cold rydberg atoms. *Phys. Rev. Lett.*, 109:233602, Dec 2012.

[17] A Grankin, E Brion, E Bimbard, R Boddeda, I Usmani, A Ourjoumtsev, and P Grangier. Quantum statistics of light transmitted through an intracavity rydberg medium. *arXiv preprint arXiv:1312.2621*, 2013.

[18] R. H. Dicke. Coherence in spontaneous radiation processes. *Phys. Rev.*, 93:99–110, Jan 1954.

[19] Michael Tavis and Frederick W. Cummings. Exact solution for an n molecule radiation field hamiltonian. *Phys. Rev.*, 170:379–384, Jun 1968.

[20] Richard W Fox, Chris W Oates, and Leo W Hollberg. 1. stabilizing diode lasers to high-finesse cavities. *Cavity-Enhanced Spectroscopies. Series: Experimental Methods in the Physical Sciences, ISBN: 9780124759879. Elsevier, vol. 40, pp. 1-46*, 40:1–46, 2003.

[21] Fabrizio Villa, Antonino Chiummo, Elisabeth Giacobino, and Alberto Bramati. High-efficiency blue-light generation with a ring cavity with periodically poled ktp. *JOSA B*, 24(3):576–580, 2007.

[22] Anthony A Tovar and Lee W Casperson. Generalized beam matrices: Gaussian beam propagation in misaligned complex optical systems. *JOSA A*, 12(7):1522–1533, 1995.

[23] Harold J Metcalf and Peter Van der Straten. *Laser cooling and trapping*. Springer, 1999.

[24] Jean Dalibard and Claude Cohen-Tannoudji. Laser cooling below the doppler limit by polarization gradients: simple theoretical models. *JOSA B*, 6(11):2023–2045, 1989.

[25] David Hunger, Tilo Steinmetz, Yves Colombe, Christian Deutsch, Theodor W Hänsch, and Jakob Reichel. A fiber fabry–perot cavity with high finesse. *New Journal of Physics*, 12(6):065038, 2010.

[26] Daniel A. Steck. Rubidium 87 d line data. available online at `http://steck.us/alkalidata`.